Research Article | Vol. 28, No. 17 / 17 August 2020 / Optics Express 25545
Optics EXPRESS

Tilt-to-length noise coupled by wavefront errors in the interfering beams for the space measurement of gravitational waves

YA ZHAO,[1,2] JIA SHEN,[2,3] CHAO FANG,[1] HESHAN LIU,[3] ZHI WANG,[1,4] AND ZIREN LUO[3,5]

[1]*Changchun Institute of Optics, Fine Mechanics and Physics Chinese Academic of Sciences, Changchun 130033, China*
[2]*University of Chinese Academy of Sciences, Beijing 100039, China*
[3]*Institute of Mechanics, Chinese Academy of Sciences, Beijing 100190, China*
[4]*wz070611@126.com*
[5]*luoziren@imech.ac.cn*

Abstract: The space-based gravitational wave detection programs, like the Laser Interferometer Space Antenna (LISA) or the Taiji program, aim to detect gravitational waves in space with a triangular constellation of three spacecraft. The unavoidable jitters of the spacecraft and the pointing will couple with the misalignment of the interfering beams into the longitudinal path length readout. This effect is called tilt-to-length (TTL) coupling, which is one of the keys to achieving the required measuring accuracy of $1pm/\sqrt{Hz}$. In terms of two phase definitions (the LISA Pathfinder (*LPF*) signal and the Average Phase (*AP*) signal), we implement the comprehensive theoretical analysis concerning the effect of aberrations on TTL coupling noise. In addition, we analytically derive that the proper lateral shift of the interfering beams relative to the detector can partly cancel out the TTL noise coupled with aberrations, especially coma and trefoil aberrations for the *AP* signal. Based on the above results, the meaningful guidance can be provided for the design and construction of the optical system in LISA or Taiji.

1. Introduction

In the spaceborne and long-baseline laser interferometers such as the Laser Interferometer Space Antenna (LISA) and the Taiji program, there are three spacecraft forming an equilateral triangle with arm lengths of millions of kilometres [1–3]. In order to successfully detect the gravitational waves, the measurement noise of the detectors needs to meet $1pm/\sqrt{Hz}$ within the frequency band from $0.1mHz$ to $1Hz$ [4,5]. This ultra-low noise level demands tightly on all aspects of these gravitational wave detectors. The science interferometer shown in Fig. 1, one of the subsystems of the interferometric system, is responsible for measuring the optical path change between the local optical bench and the optical bench on a remote spacecraft [6].

As shown in Fig. 1, the local telescope is a 4-mirror Schiefspiegler system with 80 magnification and a diameter of the primary mirror of 400 mm, and the imaging system is a Kepler system with 2.5 magnification [7]. As a result, the received flat-top beam has a diameter of $2mm$ on the detector. Furthermore, due to the spacecraft jitter and the breathing of the constellation, the received beam jitters on the detector and interferes with the static local beam at varying angles. In principle, the pupil imaging conjugate system can make the received beam imaged on the detector without beam walk and eliminate the effect of beam tilt on the change of optical path. However, it can not eliminate the TTL noise coupled with the wavefront error of the interfering beams, which are currently induced by the imperfections of the optical systems because of the manufacture and adjustment errors. The coupling coefficient is currently required to be below $25pm/\mu rad$ within $\pm 300\mu rad$ of the wavefront misalignment between the interfering beams [8].

#397097 https://doi.org/10.1364/OE.397097
Journal © 2020 Received 11 May 2020; revised 28 Jun 2020; accepted 21 Jul 2020; published 17 Aug 2020

Optics EXPRESS

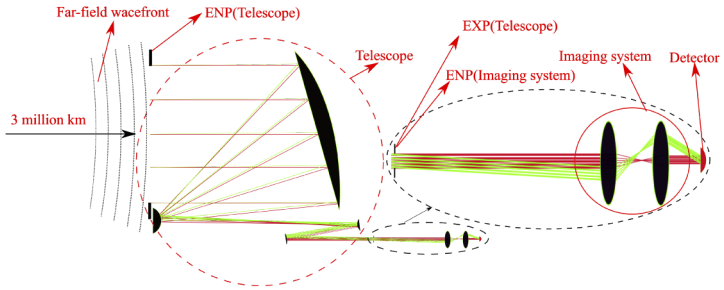

Fig. 1. The simplified diagram of the science interferometer shows the process that the far-field wavefront is clipped and narrowed through a telescope to the optical platform (lenses used to fold the optical path are omitted), and then hitting the detector through an imaging system. A pupil imaging conjugate system consists of the telescope and the imaging system. It overlaps the exit pupil (EXP) of the telescope with the entrance pupil (ENP) of the imaging system, and placing the detector at the EXP of the imaging system. The green beam of an off-axis field of view is worked by the pupil imaging conjugate system to hit the same position of the detector with the same optical path (Fermat principle) compared to the red beam of the on-axis field of view.

C P Sasso et al. analytically investigated the TTL coupling between the wavefront misalignment and the low-order aberrations of the interfering beams by extracting the phase information from the complex amplitude of a single element photodiode (SEPD) [9]. However, the quadrant photodiode (QPD) consisting of four active segments, is mostly used as the detector of the interferometric systems to obtain the DWS (differential wavefront sensing) signal for measuring small angular changes [10–12]. The phases of the four quadrants can be combined in different ways to get the overall phase of the entire QPD, and the phases obtained may be different [13].

In this paper, we analytically calculate the TTL noise coupled by aberrations including the third to the seventh order, by applying the two most common QPD path length definitions (the *AP* signal and the *LPF* signal). For the *AP* signal, we also analyze the effect of the lateral shift between the interfering beams and the detector on TTL coupling and derive an expression which theoretically explains a compensating relationship between the lateral shifts of the detector and optical lens in the experiments [14]. Meanwhile, the expressions for calculating the minimum sensitivity tilt for the TTL noise are given. Finally, we carry out Monte Carlo simulations for the *LPF* signal and the three kinds of *AP* signals with three different settings of the lateral shift by trying arbitrary wavefront errors. The results intuitively show that the *AP* signal can more greatly reduce the TTL noise coupled with aberrations compared to the *LPF* signal, and introducing the appropriate lateral shift of the interfering beams on the detector can further reduce the TTL coupling. The AP signal with $\lambda/10$ wavefront error of the interfering beams is better than the LPF signal with $\lambda/20$ wavefront error when other states are the same. Therefore, the analyses C P Sasso et al. performed in [9,15] may exaggerate the influence of aberrations on the TTL noise to put forward too high demand for wavefront quality.

2. Optical model

The far-field wavefront is narrowed by the off-axis telescope as a flat-top beam, which then superimposing with the local Gaussian beam pass the imaging system together to interfere on the QPD [16]. By proper adjustment, the relative position between the two interfering beams can go below microns level. For the sake of simplicity, we assume that the centers of the two beams coincide and set the center as the coordinate origin shown in Fig. 2. Consequently, the

Optics EXPRESS

local Gaussian beam on the detector can be written as (in polar coordinates):

$$E_1(r,\theta,z,t) = e^{\frac{-r^2}{\omega(z)^2}} e^{-ik\left[\frac{r^2}{2R(z)}+w_1(r,\theta)\right]+i\omega_1 t}, \tag{1}$$

where $k = 2\pi/\lambda$ is the wavenumber, λ is the wavelength. (r,θ) is the polar coordinate on the detector plane, $\omega(z) = \omega_0\sqrt{1+(\frac{z}{z_0})^2}$ is the spot size on the detector, where ω_0 is the waist size, z is the distance away from the waist position, $z_0 = \pi\omega_0^2/\lambda$ is the Rayleigh distance. $R(z) = z\left[1+(z_0/z)^2\right]$ is the radius of the wavefront curvature. The phase term $\frac{-r^2}{2R(z)}$ is similar to defocus, and whether it is equal to 0 depends on whether z is equal to 0. $w_1(r,\theta)$ represents the wavefront error of the local beam created by defective optical elements. ω_1 is the angular frequency.

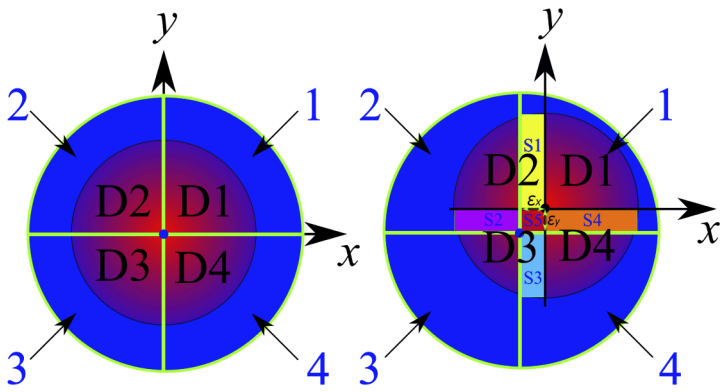

Fig. 2. The interfering beams hit centrally (left) and eccentrically (right) on the QPD. In the pictures, $D1$, $D2$, $D3$ and $D4$ represent the valid integral regions in the four Cartesian coordinate quadrants. Blue numbers 1,2,3,4 indicate the four segments in the QPD, respectively. ϵ_x and ϵ_y are the eccentricities in the x-direction and y-direction between the interfering beam and the QPD. $S1$, $S2$, $S3$, $S4$ and $S5$ stand for the changed effective integral regions of the four segments induced by the eccentricity.

The flat-top beam on the detector can be derived as (in polar coordinates):

$$E_2(r,\theta,t) = \begin{cases} e^{-ik[r\alpha\cos(\theta-\theta_\alpha)+w_2(r,\theta)]+i\omega_2 t} & r \le r_0 \\ 0 & \text{else} \end{cases}, \tag{2}$$

where α is the small tilt angle of the beam about an axis that is orthogonal to a line making an angle of θ_α with the x axis on the detector plane, r_0 is the radial dimension of the flat-top beam. $w_2(r,\theta)$ also represents the wavefront error of the flat-top beam caused by defective optical elements including the off-axis telescope. ω_2 is the angular frequency.

Provide that the interfering beams can be detected without clipping, it is easy to extract the phase from an integration of the complex overlap term over the detection area. Since the phase is time-independent, we set $t = 0$ and the integrand becomes:

$$O_{ovi}(r,\theta) = \int_S E_1 E_2^* dr^2 = \int_S e^{\frac{-r^2}{\omega(z)^2}} e^{ikW(r,\theta)} dr^2, \tag{3}$$

where $W(r,\theta) = r\alpha\cos(\theta-\theta_\alpha) + \Delta w(r,\theta)$, represents the total wavefront error including tilt, and $\Delta w(r,\theta) = w_2(r,\theta) - w_1(r,\theta) - \frac{r^2}{2R(z)}$, denotes the static wavefront error of the interfering beams.

Optics EXPRESS

Then the phase information is extracted from the argument of (3). In this paper, the range of the static wavefront error $\Delta w(r,\theta)$ discussed is less than $0.1064\mu m$, and the range of the tilt angle α discussed is within $\pm 300\mu rad$. So based on computational accuracy, the exponential term $e^{ikW(r,\theta)}$ is approximate to:

$$e^{ikW(r,\theta)} \approx 1 + ikW(r,\theta) - \frac{1}{2}k^2W(r,\theta)^2 - \frac{i}{6}k^3W(r,\theta)^3. \tag{4}$$

As shown in Fig. 2, the complex amplitude for every segment of such a QPD can be calculated. And there are the two most common ways to combine the complex amplitudes of the four segments in the current projects. The first phase definition selected by LISA Pathfinder is the *LPF* signal, which first sums the complex amplitudes of each segment of the QPD and then calculates the argument from the sum [13]:

$$\phi_{LPF} = \arg\left(\sum_{n=1}^{4} O_{ovi}^{n}\right). \tag{5a}$$

Here, the slit of the QPD is not considered in the following calculations because the effect of the ten microns scale slit gap of the universal QPD on the total complex amplitude is negligible. As a result, we can directly integrate the entire circle to calculate ϕ_{LPF} (And $\arg x$ is approximated as $Im(x)/Re(x)$ in the calculation):

$$\begin{aligned}\phi_{LPF} &= \arg\left[\int_0^1 \rho e^{-\rho^2/\omega_r^2}\left(\int_0^{2\pi} e^{ikW(\rho,\theta)}d\theta\right)d\rho\right] \\ &\approx \arg(a_0 + ia_1 - a_2 - ia_3) \\ &\approx \frac{(a_1 - a_3)(a_0 + a_2)}{a_0^2},\end{aligned} \tag{5b}$$

where $\omega_r = \omega(z)/r_0$, $\rho = r/r_0$ and

$$a_n = \frac{1}{n!}\int_0^1 \rho e^{-\rho^2/\omega_r^2}\left(\int_0^{2\pi} [kW(\rho,\theta)]^n d\theta\right)d\rho. \tag{5c}$$

The second phase definition is the *AP* signal, which first takes the resulting phase of each segment of the QPD and then averages it. By assuming $\sqrt{\epsilon_x^2 + \epsilon_y^2} \ll r_0$, the shape of *Si* areas can be regarded as a rectangle, as shown in Fig. 2. Therefore, it is more suitable to calculate the complex amplitudes of the *Si* areas with Cartesian coordinates. And the exponential term $e^{ikW(x,y)}$ is approximated up to the first order because the *Si* areas are very small:

$$e^{ikW(x,y)} \approx 1 + ikW(x,y). \tag{6}$$

The effective integral regions of the four segments in the QPD are shown in the Fig. 2. Accordingly, the calculations of the complex amplitudes of the four segments are given in (7a~7d):

$$O_{ovi}^{1} = \int_{D1} O_{ovi}(r,\theta) + \int_{S1+S4+S5} O_{ovi}(x,y), \tag{7a}$$

$$O_{ovi}^{2} = \int_{D2} O_{ovi}(r,\theta) - \int_{S1} O_{ovi}(x,y) + \int_{S2} O_{ovi}(x,y), \tag{7b}$$

$$O_{ovi}^{3} = \int_{D3} O_{ovi}(r,\theta) - \int_{S2+S3+S5} O_{ovi}(x,y), \tag{7c}$$

Optics EXPRESS

$$O_{ovi}^{4} = \int_{D4} O_{ovi}(r,\theta) - \int_{S4} O_{ovi}(x,y) + \int_{S3} O_{ovi}(x,y). \tag{7d}$$

Here we take (7a) as an example to show the phase calculation process of the first segment of the QPD. The calculation of the complex amplitudes of the $D1$ area is shown in (8a) and (8b).

$$O_{ovi}^{D1} \approx d_0 + id_1 - d_2 - id_3, \tag{8a}$$

$$d_n = \frac{1}{n!}\int_0^1 \rho e^{-\rho^2/\omega_r^2}\left(\int_0^{\pi/2} [kW(\rho,\theta)]^n d\theta\right) d\rho, \tag{8b}$$

When calculating the complex amplitudes of the Si area, ϵ_x and ϵ_y are expressed via the polar vector $\epsilon, \theta_\epsilon$ ($\epsilon_x = \epsilon * \cos\theta_\epsilon$, $\epsilon_y = \epsilon * \sin\theta_\epsilon$, $\theta_\epsilon \in [0, 2\pi]$):

$$O_{ovi}^{S1+S4+S5} \approx s_0 + is_1, \tag{8c}$$

$$\begin{aligned} s_n = &\int_0^1 \int_{\epsilon_r\cos\theta_\epsilon}^0 e^{-(x_r^2+y_r^2)/\omega_r^2}[kW(x_r,y_r)]^n dx_r dy_r \\ &+ \int_{\epsilon_r\sin\theta_\epsilon}^0 \int_0^1 e^{-(x_r^2+y_r^2)/\omega_r^2}[kW(x_r,y_r)]^n dx_r dy_r \\ &+ \int_{\epsilon_r\sin\theta_\epsilon}^0 \int_{\epsilon_r\cos\theta_\epsilon}^0 e^{-(x_r^2+y_r^2)/\omega_r^2}[kW(x_r,y_r)]^n dx_r dy_r, \end{aligned} \tag{8d}$$

where $x_r = x/r_0$, $y_r = y/r_0$, $\epsilon_r = \epsilon/r_0$ are the normalized parameters. Combining (8a) and (8c), we can get the complex amplitudes of the first segment of the QPD:

$$O_{ovi}^{1} \approx d_0 + s_0 - d_2 + i(d_1 + s_1 - d_3)). \tag{8e}$$

For the complex amplitudes of the other three segments, we just change the integral regions of (8a~8d) according to (7b~7d) to calculate the expressions similar to (8e). Eventually, the AP signal can be expressed as:

$$\phi_{AP} \approx \frac{1}{4}\frac{Im(\prod_{n=1}^{4} O_{ovi}^{n})}{Re(\prod_{n=1}^{4} O_{ovi}^{n})}. \tag{8f}$$

It is easy to notice that the LPF signal is insensitive to the static lateral displacement ϵ. In contrast, the lateral position offset of the interfering beams on the QPD will change the complex amplitude of each segment on the QPD and consequently alter the AP signal. However, it does not mean that the AP signal is a bad phase definition. On the contrary, this character can provide the AP signal a certain degree of freedom to offset the phase noises induced by aberrations, which will be verified theoretically in the next section.

3. The coupling of TTL noise with aberrations

3.1. Simple analysis with the spherical aberration and the coma of Seidel aberrations

First, simple analytical expressions are derived to visually show the coupling relationship between the phase noises and the aberrations for the LPF signal and the AP signal. Here we set $R(z) = \infty$, and choose the radial symmetric spherical aberration and the asymmetric coma in Seidel aberrations to form $\Delta w(r,\theta)$. As a result, $W(r,\theta)$ and $W(x,y)$ become:

$$W(r,\theta) = r\alpha\cos(\theta - \theta_\alpha) + A_c r^3\cos(\theta - \theta_c) + A_s r^4, \tag{9a}$$

$$W(x,y) = \alpha(x\cos\theta_\alpha + y\sin\theta_\alpha) + A_c(x^2+y^2)(x\cos\theta_c + y\sin\theta_c) + A_s(x^2+y^2)^2, \tag{9b}$$

where A_c and A_s represent the coefficients of the coma and the spherical aberration, respectively, and the coma is symmetric about a line making angle of θ_c with the x axis. Next, we carry out the

Optics EXPRESS

symbolic calculations of the integration (5c) and (5b) by utilizing Mathematica (the Mathematica code is available in the supplementary material as we shown in Code 1 [17]). Because we focus on the coupling between the small rotation angle α and the phase, the terms unrelated and higher than second order of α are omitted during the simplification. Therefore, the longitudinal pathlength signal (LPS) LPS_{LPF} of the LPF signal is (ϕ_{LPF}/k):

$$LPS_{LPF} \approx b_1 * A_c A_s \alpha + b_2 * A_s \alpha^2, \tag{10a}$$

$$b_1 = -\frac{k^2\left(20e^{\frac{2}{\omega_r^2}}\omega_r^8 + 4\left(5\omega_r^8 + 4\omega_r^6 + \omega_r^4\right) - e^{\frac{1}{\omega_r^2}}\left(40\omega_r^8 + 16\omega_r^6 + 8\omega_r^4 + 4\omega_r^2 + 1\right)\right)\cos\left(\theta_c - \theta_\alpha\right)}{2\left(e^{\frac{1}{\omega_r^2}} - 1\right)^2}, \tag{10b}$$

$$b_2 = -\frac{k^2\left(4e^{\frac{2}{\omega_r^2}}\omega_r^6 + 2\left(2\omega_r^6 + \omega_r^4\right) - e^{\frac{1}{\omega_r^2}}\left(8\omega_r^6 + 2\omega_r^4 + 2\omega_r^2 + 1\right)\right)}{4\left(e^{\frac{1}{\omega_r^2}} - 1\right)^2}. \tag{10c}$$

Meanwhile, the LPS_{AP} of the AP signal is:

$$LPS_{AP} \approx \left[p_1 * A_s A_c + (p_1^{\epsilon 1} + p_1^{\epsilon 2} * A_s^2) * \epsilon_r\right]\alpha + p_2 * A_s \alpha^2, \tag{11a}$$

where the expressions of p_1 and p_2 are too long, thus being denoted by the power series of ω_r with the coefficients $p1_n$ and $p2_n$, as shown in (11b) and (11c), respectively. (the full expressions can be shown by the supplementary material as we shown in Code 1 (Ref. [17])).

$$p_1 = k^2 \cos(\theta_\alpha - \theta_c) \sum_{n=0}^{8} p1_n \omega_r^n, \tag{11b}$$

$$p_2 = \sum_{n=0}^{6} p2_n k^2 \omega_r^n, \tag{11c}$$

The coefficient of α^2 contains one term concerning the lateral shift ϵ_r, and this term is so negligible that can be omitted when ϵ_r is within ± 0.02. $p_1^{\epsilon 1}$ (11d) is independent of aberrations. $p_1^{\epsilon 2}$ (11e) is also denoted by the power series of ω_r with the coefficients $p1\epsilon 2_n$ (the full expressions are provided in the supplementary material as we shown in Code 1 (Ref. [17])).

$$p_1^{\epsilon 1} = \frac{2\cos(\theta_\alpha - \theta_\epsilon)e^{\frac{1}{\omega_r^2}}\,\mathrm{erf}\left(\frac{1}{\omega_r}\right)\left(\sqrt{\pi}e^{\frac{1}{\omega_r}}\omega_r \mathrm{erf}\left(\frac{1}{\omega_r}\right) - 2\right)}{\pi^{3/2}\left(e^{\frac{1}{\omega_r^2}} - 1\right)^2 \omega_r}, \tag{11d}$$

$$p_1^{\epsilon 2} = k^2 \cos(\theta_\alpha - \theta_\epsilon) \sum_{n=-1}^{8} p1\epsilon 2_n \omega_r^n. \tag{11e}$$

The Eqs. (10b) and (11b) indicate that the coupling degree of the coma A_c with TTL noise depends on the cosine of the included angle between θ_α and θ_c whatever for LPS_{LPF} or LPS_{AP}. When we set $A_s = A_c = 0$ to eliminate the wavefront mismatch of the interfering beams, LPS_{LPF} is free for tilting, but LPS_{AP} has a linear coupling relation with the angle α because of the lateral shift ϵ_r. Similarly, the coupling degree of the lateral shift ϵ_r with TTL noise for LPS_{AP} depends on the cosine of the included angle between θ_α and θ_ϵ.

Optics EXPRESS

The coupling coefficients δ_{LPS}^{LPF} and δ_{LPS}^{AP}, calculated by taking the derivatives of (10a) and (11a) with respect to α, characterize the sensitivity of *LPS* to the tilting angle.

$$\delta_{LPS}^{LPF} = \frac{d(LPS_{LPF})}{d(\alpha)} = b_1 * A_c A_s + 2b_2 * A_s \alpha, \tag{12a}$$

$$\delta_{LPS}^{AP} = \frac{d(LPS_{AP})}{d(\alpha)} = p_1 * A_s A_c + (p_1^{\epsilon 1} + p_1^{\epsilon 2} * A_s^2) * \epsilon_r + 2p_2 * A_s \alpha. \tag{12b}$$

It is worth noting that the constant term of δ_{LPS}^{AP} can be eliminated if ϵ_r satisfies:

$$\epsilon_r^{opt} = -\frac{p_1 * A_s A_c}{(p_1^{\epsilon 1} + p_1^{\epsilon 2} A_s^2)}, \tag{13}$$

where $\epsilon_r^{opt} = \epsilon_{opt}/r_0$ is the normalized optimal lateral shift. Equation (13) indicates that the component of the lateral shift in the direction which is orthogonal to the jittering axis of the beam, works for reducing the TTL noise coupled with the aberrations. Meanwhile, we can obtain the two optimal angles α_{LPF}^0 and α_{AP}^0, which can minimize δ_{LPS}^{LPF} and δ_{LPS}^{AP} to 0, respectively:

$$\alpha_{LPF}^0 = -\frac{b_1 * A_c A_s}{2b_2 * A_s}, \tag{14a}$$

$$\alpha_{AP}^0 = -\frac{p_1 * A_s A_c + (p_1^{\epsilon 1} + p_1^{\epsilon 2} A_s^2) * \epsilon}{2p_2 * A_s}. \tag{14b}$$

Assuming that $\theta_\alpha = \theta_\epsilon = \theta_c = 0$ and $\omega(z) = r_0 = 1mm$ to consider one-dimensional situation, the above results are intuitively shown on Fig. 3. By adjusting ϵ to ϵ_{opt}, the TTL noise coupled with the coma can be surely eliminated for the AP signal, and α_{AP}^0 simultaneously becomes 0. And if ϵ is not too large, it is obvious that the *AP* signal is less sensitive than the *LPF* signal for the TTL noise coupled with aberrations.

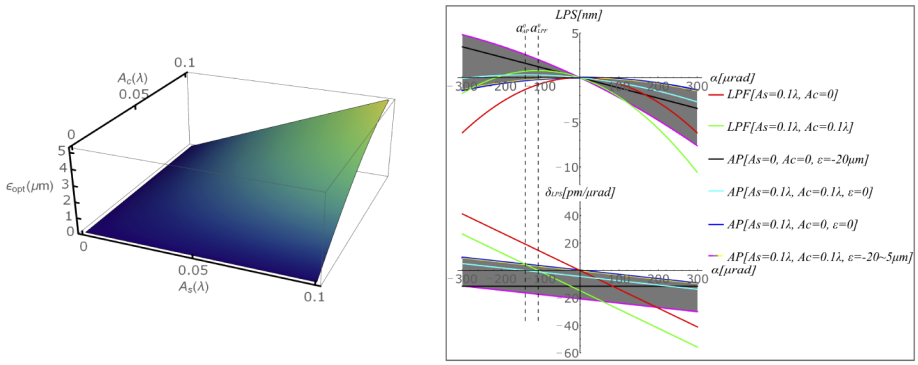

Fig. 3. Left: $\epsilon_{opt}(13)$ changing with A_s and A_c. Right: LPS_{LPF}, LPS_{AP} and their coupling coefficients δ_{LPS}^{LPF}, δ_{LPS}^{AP} with different values of A_s and A_c, versus the wavefront tilt α.

Optics EXPRESS

3.2. The comprehensive theoretical analysis with Zernike polynomials

An excellent choice as basis functions for representing functions such as wavefronts is Zernike circle polynomials, which are orthogonal over a unit circle in the form [18]:

$$Z_i(\rho,\theta) = \begin{cases} \sqrt{2(n+1)}R_n^m(\rho)\cos(m\theta) & \text{i is even and } m \neq 0 \\ \sqrt{2(n+1)}R_n^m(\rho)\sin(m\theta) & \text{i is odd and } m \neq 0 \\ \sqrt{n+1}R_n^0(\rho) & m = 0 \end{cases}, \tag{15}$$

where $R_n^m(\rho)$ (16) is the radial polynomial, n and m are positive integers, and $n - m \geq 0$. $\rho = r/r_0$ is the normalized radial coordinate. The index i is a polynomial-ordering number and a function of n and m.

$$R_n^m(\rho) = \sum_{s=0}^{(n-m)/2} \frac{(-1)^s(n-s)!}{s!(\frac{n+m}{2}-s)!(\frac{n+m}{2}-s)!}\rho^{n-2s}. \tag{16}$$

There are several ways of representing the Zernike polynomials, with one difference being the ordering of terms. Here, the Fringe Zernike polynomials, currently used by several vendors of interferometers and interferometric data analysis software, are chosen in the analysis. In order to fully characterise the manufacturing and adjustment errors of the optical systems, the first 25 terms of the Fringe Zernike polynomials are used to fit the wavefront error of the interfering beams (the piston term being omitted). Furthermore, except the defocus term and three spherical aberration terms, the cosine and sine terms of other Zernike aberrations are combined to represent the magnitudes and orientations of these aberrations. For example, when both x and y Zernike tilts are used to present the wavefront tilt, the aberration may be written as the form:

$$a_2Z_2(\rho,\theta) + a_3Z_3(\rho,\theta) = A_1^{Ti}\rho\cos(\theta - \theta_{Ti}), \tag{17}$$

showing a wavefront tilt of magnitude $A_1^{Ti} = r_0\alpha = 2\sqrt{a_2^2 + a_3^2}$ about an axis that is orthogonal to a line making an angle of $\theta_{Ti} = \theta_\alpha = \tan^{-1}(a_3/a_2)$ with the x axis. Where a_i is the expansion coefficient before combination and A_j^{aber} is the magnitude of the aberration after combination (its subscript is the serial number j and superscript is the abbreviation of the corresponding aberration). The complete orthonormal Zernike polynomials $Z_j(\rho,\theta)$ in polar coordinates and $Z_j(x,y)$ in Cartesian coordinates are given in Table 1, where θ_{aber} presents an orientation angle of the corresponding aberration inclined with the x axis and its subscript is the abbreviation of the corresponding aberration. The effect of the phase term $\frac{-r^2}{2R(z)}$ can be represented by the defocus Zernike term. As a result, the wavefront error can be presented as:

$$W(\rho,\theta) = \sum_j^{14} A_j^{aber}Z_j(\rho,\theta), \tag{18a}$$

$$W(x,y) = \sum_j^{14} A_j^{aber}Z_j(x,y). \tag{18b}$$

The expansion coefficients A_j^{aber} are given by:

$$A_j^{aber} = \frac{1}{\pi}\int_0^1\int_0^{2\pi} W(\rho,\theta)Z_j(\rho,\theta)\rho d\rho d\theta \tag{19}$$

The aberration variance is given by:

$$\delta_W^2 = \sum_j (A_j^{aber})^2, \tag{20}$$

Optics EXPRESS

where δ_W can be regarded as the root-mean-square (RMS) value of the wavefront error because the piston term a_0 is not included here.

After (9a) and (9b) are replaced by (18a) and (18b), δ_{LPS}^{LPF} and the corresponding optimal tilt angle α_{LPF}^{0} can be expressed as:

$$\delta_{LPS}^{LPF} = B_1 + 2B_2\alpha, \tag{21a}$$

$$\alpha_{LPF}^{0} = -\frac{B_1}{2B_2}, \tag{21b}$$

$$B_1 = \sum_{n=1}^{29} B1_n * A1_n^{LPF}, \tag{21c}$$

$$B_2 = \sum_{n=1}^{7} B2_n * A2_n^{LPF}, \tag{21d}$$

where B_1 (21c) is the sum of 29 factors $A1_n^{LPF}$ (21g) with the coefficients $B1_n$, the 21 factors of which are the pairwise combinations between the three coma terms and the group AA_1^{LPF} (21e) including the four spherical terms (including defocus) and the three astigmatism terms, and the other 8 factors are the pairwise combinations between the two trefoil terms and the group AA_2^{LPF} (21f) including the three astigmatism terms and the primary tetrafoil term. B_2 (21d) is the sum of 7 factors $A2_n^{LPF}$ (21h) including the 7 terms in the group AA_1^{LPF} with the coefficients $B2_n$ (21h).

$$AA_1^{LPF} \Longrightarrow \left\{A_2^{DE}, A_5^{PS}, A_9^{SS}, A_{14}^{TS}, A_3^{PA}, A_7^{SA}, A_{12}^{TA}\right\}, \tag{21e}$$

$$AA_2^{LPF} \Longrightarrow \left\{A_3^{PA}, A_7^{SA}, A_{12}^{T^A}, A_{10}^{PTE}\right\}, \tag{21f}$$

$$A1_n^{LPF} \Longrightarrow \left\{\{A_4^{PC}, A_8^{SC}, A_{13}^{TC}\} * AA_1^{LPF}, \{A_6^{PTR}, A_{11}^{STR}\} * AA_2^{LPF}\right\}, \tag{21g}$$

$$A2_n^{LPF} \Longrightarrow AA_1^{LPF}. \tag{21h}$$

Because of too many factors in (18a) and (18b), it is very hard to directly calculate δ_{LPS}^{AP} by using the Eq. (8a). Therefore, we expand $\prod_{n=1}^{4} O_{ovi}^{n}$ and neglect some factors to reduce the amount of calculation through only considering the terms that are not higher than the second order of α and the first order of ϵ_r (the Mathematica codes of the specific simplification process are shown in the supplementary material as we shown in Code 1 (Ref. [17])). As a result, δ_{LPS}^{AP} and the corresponding optimal tilt angle α_{AP}^{0} can be expressed as:

$$\delta_{LPS}^{AP} = \left[P_1 + (P_1^{\epsilon 1} + P_1^{\epsilon 2}) * \epsilon_r\right] + 2\left(P_2 + P_2^{\epsilon} * \epsilon_r\right)\alpha, \tag{22a}$$

$$\alpha_{AP}^{0} = -\frac{\left[P_1 + (P_1^{\epsilon 1} + P_1^{\epsilon 2}) * \epsilon_r\right]}{\left(P_2 + P_2^{\epsilon} * \epsilon_r\right)}, \tag{22b}$$

$$P_1 = \sum_{n=1}^{40} P1_n * A1_n^{AP}, \tag{22c}$$

$$P_2 = \sum_{n=1}^{8} P2_n * A2_n^{AP}, \tag{22d}$$

$$P_1^{\epsilon 1} = p1\epsilon 1, \tag{22e}$$

$$P_1^{\epsilon 2} = \sum_{n=1}^{51} P1\epsilon 2_n * A1\epsilon_n, \tag{22f}$$

Table 1. The fourteen Zernike aberrations consist of The first 25 terms of Fringe Zernike polynomials.

i	j	$Z_j(\rho,\theta)$	$Z_j(x,y)$	Aberration name
2,3	1	$\rho\cos(\theta-\theta_\alpha)$	$x\cos(\theta_\alpha)+y\sin(\theta_\alpha)$	Tilt
4	2	$\sqrt{3}(2\rho^2-1)$	$\sqrt{3}[2(x^2+y^2)-1]$	Defocus
5,6	3	$\sqrt{6}\rho^2\cos(2\theta-(\theta_{PA}))$	$\sqrt{6}[2xy\sin(\theta_{PA})+(x^2-y^2)\cos(\theta_{PA})]$	Primary astigmatism
7,8	4	$\sqrt{8}(3\rho^3-2\rho)\cos(\theta-(\theta_{PC}))$	$\sqrt{8}(x\cos(\theta_{PC})+y\sin(\theta_{PC}))(3\rho^2-2)$	Primary coma
9	5	$\sqrt{5}(6\rho^4-6\rho^2+1)$	$\sqrt{5}(6\rho^4-6\rho^2+1)$	Primary spherical
10,11	6	$\sqrt{8}\rho^3\cos(3\theta-\theta_{PTR})$	$\sqrt{8}[x\cos(\theta_{PTR})(x^2-3y^2)+y\sin(\theta_{PTR})(3x^2-y^2)]$	Primary trefoil
12,13	7	$\sqrt{10}(4\rho^4-3\rho^2)\cos(\theta-\theta_{SA})$	$\sqrt{10}(2xy\sin(\theta_{PA})+(x^2-y^2)\cos(\theta_{SA}))(4\rho^2-3)$	Secondary astigmatism
14,15	8	$\sqrt{5}(10\rho^5-12\rho^3+3\rho)\cos(2\theta-\theta_{SC})$	$\sqrt{8}(x\cos(\theta_{SC})+y\sin(\theta_{SC}))(10\rho^4-12\rho^2+3)$	Secondary coma
16	9	$\sqrt{5}(20\rho^6-30\rho^4+12\rho^2-1)$	$\sqrt{5}(20\rho^6-30\rho^4+12\rho^2-1)$	Secondary spherical
17,18	10	$\sqrt{5}\rho^4\cos(4\theta-\theta_{PTE})$	$(\rho^4-8x^2y^2)\cos(\theta_{PTE})+4xy(x^2-y^2)\sin(\theta_{PTE})$	Primary tetrafoil
19,20	11	$\sqrt{8}(5\rho^5-4\rho^3)\cos(3\theta-\theta_{STR})$	$\sqrt{8}(x\cos(\theta_{PTR})(x^2-3y^2)+y\sin(\theta_{PTR})(3x^2-y^2))(5\rho^2-4)$	Secondary trefoil
21,22	12	$\sqrt{5}(15\rho^6-20\rho^4+6\rho^2)\cos(2\theta-\theta_{TA})$	$\sqrt{10}(2xy\sin(\theta_{PA})+(x^2-y^2)\cos(\theta_{SA}))(15\rho^4-20\rho^2+6\rho)$	Tertiary astigmatism
23,24	13	$\sqrt{5}(35\rho^7-60\rho^5+30\rho^3-4\rho)\cos(2\theta-\theta_{TC})$	$\sqrt{8}(x\cos(\theta_{SC})+y\sin(\theta_{SC}))(35\rho^7-60\rho^4+30\rho^2-4)$	Tertiary coma
25	14	$\sqrt{5}(70\rho^8-140\rho^6+90\rho^4-20\rho^2+1)$	$\sqrt{5}(70\rho^8-140\rho^6+90\rho^4-20\rho^2+1)$	Tertiary spherical

Optics EXPRESS

$$P_2^{\epsilon} = \sum_{n=1}^{5} P2\epsilon_n * A2\epsilon_n, \tag{22g}$$

where P_1 (22c) is the sum of 40 factors $A1_n^{AP}$ (22j) with the coefficients $P1_n$, which are the pairwise combinations between the group AA_1^{AP} (22h) including the four spherical terms, the three astigmatism terms and the primary tetrafoil term and the group AA_2^{AP} (22i) including the three coma terms and the two trefoil terms. P_2 (22d) is the sum of 8 factors $A2_n^{AP}$ (22k) including the 8 terms in the group AA_1^{AP} with the coefficients $P2_n$. $P_1^{\epsilon 1}$ (22e) is equal to $p_1^{\epsilon}1$ (11d), which is independent of aberrations. $P_1^{\epsilon 2}$ (22f) is the sum of 51 factors $A1\epsilon_n$ (22l) with the coefficients $P1\epsilon 2_n$, the 36 factors of which are the pairwise combinations (where any two different terms are combined in pairs and every term can also be combined with itself in pairs to form the pairwise combinations) of the group AA_1^{AP}, and the other 15 factors are formed in the same way of pairwise combinations of the group AA_2^{AP}. P_2^{ϵ} (22g) is the sum of 5 factors $A2\epsilon_n$ (22m) including the 5 terms in the group AA_2^{AP} with the coefficients $P2\epsilon_n$.

$$AA_1^{AP} \Longrightarrow \left\{A_2^{DE}, A_5^{PS}, A_9^{SS}, A_{14}^{TS}, A_3^{PA}, A_7^{SA}, A_{12}^{TA}, A_{10}^{PTE}\right\}, \tag{22h}$$

$$AA_2^{AP} \Longrightarrow \left\{A_4^{PC}, A_8^{SC}, A_{13}^{TC}, A_6^{PTR}, A_{11}^{STR}\right\}, \tag{22i}$$

$$A1_n^{AP} \Longrightarrow \left\{AA_1^{AP} * AA_2^{AP}\right\}, \tag{22j}$$

$$A2_n^{AP} \Longrightarrow AA_1^{AP}, \tag{22k}$$

$$A1\epsilon_n \Longrightarrow \left\{AA_1^{AP} * AA_1^{AP}, AA_2^{AP} * AA_2^{AP}\right\}, \tag{22l}$$

$$A2\epsilon_n \Longrightarrow AA_2^{AP}. \tag{22m}$$

Like the expression (10b) or (11b), the coefficients $B1_n$, $B2_n$, $P1_n$ and $P2_n$ are the functions of the normalized radius ω_r and the cosine of the add and subtract combination between θ_α and θ_{aber} (corresponding to the aberration terms of $A1_n$ and $A2_n$). Like the expression (11d) or (11e), $P1\epsilon 2_n$, $P2\epsilon_n$ are the functions of the normalized radius ω_r, the cosine of the add and subtract combination among θ_α, θ_ϵ and θ_{aber} (corresponding to the aberration terms of $A1\epsilon_n$ and $A2\epsilon_n$). The texts of these coefficients are not shown here due to limited space. But providing that the cosine terms are equal to 1 by setting θ_α, θ_ϵ, and other θ_{aber} to be 0, and all the magnitudes A_j^{aber} are equal to $\lambda/10$, Fig. 4 shows every sub-term of B_1, P_1 (left) and $2 * B_2 * \alpha_{max}$, $2 * P_2 * \alpha_{max}$ (middle) versus the normalized radius ω_r. And the right of Fig. 4 shows $P_1^{\epsilon 1}$, $P_1^{\epsilon 2}$, and $2 * P_2^{\epsilon} * \alpha_{max}$ (right) versus the lateral shift ϵ_r ($\omega_r = 1$) (for consistency, B_2, P_2 and P_2^{ϵ} multiplied by $2\alpha_{max}$, where $\alpha_{max} = 300\mu rad$).

In general, we can notice that the sub-term values of B_1, $2 * B_2 * \alpha_{max}$ are larger than P_1, $2 * P_2 * \alpha_{max}$, respectively. And it is also worth noting that in the coefficients of ϵ_r, the three largest sub-terms are $P_1^{\epsilon 1}$ and the two terms about $(A_2^{DE})^2$, $A_2^{DE} * A_5^{PS}$ of $P_1^{\epsilon 2}$, whose cosine terms are all $\cos(\theta_\alpha - \theta_\epsilon)$. Consequently, P_2^{ϵ} can be ignored for its smaller values and we set $\theta_\epsilon = \theta_\alpha$ when calculating the normalized optimal lateral shift ϵ_r^{opt} shown as:

$$\epsilon_r^{opt} = -\frac{P_1}{P_1^{\epsilon 1} + P_1^{\epsilon 2}}. \tag{23}$$

Optics EXPRESS

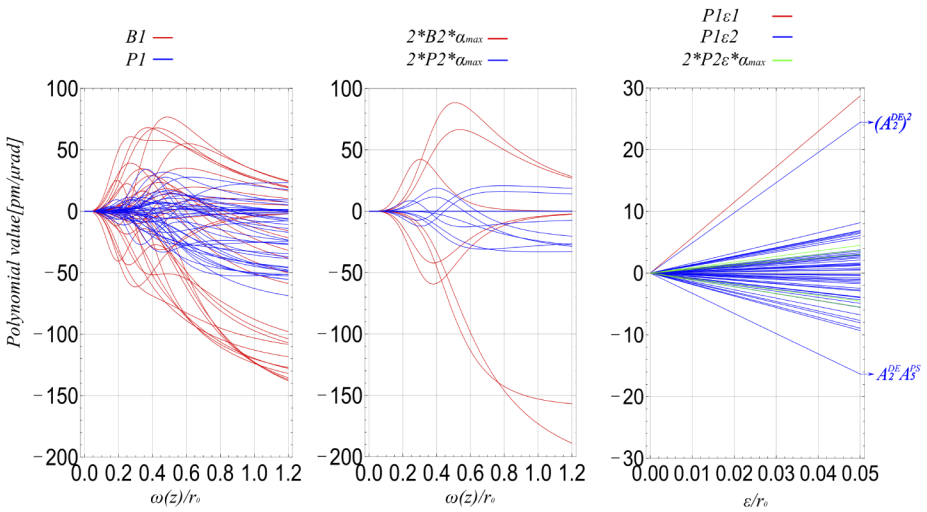

Fig. 4. Left: every sub-term of B_1, P_1 versus ω_r. Middle: every sub-term of $B_2 * 2\alpha_{max}$, $P_2 * 2\alpha_{max}$ versus ω_r. Right: every sub-term of $P_1^{\epsilon 1}$, $P_1^{\epsilon 2}$ and P_2^{ϵ} versus ϵ_r.

4. Results

Because the actual $W(\rho, \theta)$ spectrum (18a) is not available, it is necessary to predict the TTL noise coupled with aberrations under the different constraints of $\delta_W(20)$ by adopting the Monte Carlo simulation for the analytical results of the previous section.

To give an example, we set a situation that the beam wavelength $\lambda = 1064nm$, the radius of the flat-top beam and the spot size of the Gaussian beam on the detector $\omega(z) = r_0 = 1mm$. Meanwhile, the coefficients A_j^{aber} (except A_1^{Ti}) are randomly generated according to (20) in the constraint of $\delta_W = \lambda/20 = 53.2nm$ and the orientation angles θ_{aber} (except θ_{Ti}) are randomly generated in the interval of $[0, 2\pi]$. Figure 5 (left) shows a randomly generated wavefront, and the right of Fig. 5 indicates that the value of ϵ_{opt} depends on the orientation of the wavefront tilt due to the random orientation angles θ_{aber} of some aberrations in this wavefront sample. Figure 6 and 7 show the absolute values of two kinds of δ_{LPS}^{AP} and δ_{LPS}^{LPF} versus both the horizontal tilt angle $\alpha_x = \alpha\cos(\theta_\alpha)$ and the vertical tilt angle $\alpha_y = \alpha\sin(\theta_\alpha)$, respectively. As expected, the optimal lateral shift can slightly reduce δ_{LPS}^{AP}. Meanwhile, the red dotted lines in the three pictures indicate that the distributions of the optimal wavefront tilts are one or two continuous curves and are different for three kinds of situations.

It is noticed that the premises of the parabolic approximation used in the previous theoretical analysis are that $|kW(\rho, \theta)| \ll 1$ and $\epsilon_r \ll 1$. In order to verify the validity of the approximations for the large misaligment, the wavefront error and the lateral shift, we calculate the residual error δ_{approx} (24) between the approximate analytical solutions LPS_{approx} and the corresponding numerical simulations LPS_{num} of the LPF signal and the AP signal with 10^4 arbitrary wavefront samples (the analytical solutions of the LPS signals are the primitive functions of (21a) and (22a) without the constant term). Figure 8 shows that, the mean values of δ_{approx}^{LPF} and δ_{approx}^{AP} are -5.7% and 2.4%, with the standard deviations of 13% and 10%, respectively.

$$\delta_{approx} = (LPS_{approx} - LPS_{num})/LPS_{num}. \tag{24}$$

In the following analysis, we first carry out Monte Carlo algorithm to generate 10^4 groups of A_j^{aber} (expect A_1^{Ti}) and θ_{aber} (including $\theta_\alpha = \theta_{Ti}$), respectively, in the cases of $\lambda/40$, $\lambda/20$ and $\lambda/10$ of δ_W. Next, we use the wavefront tilt $\alpha = A_1^{Ti}$ to maximize $|\delta_{LPS}^{AP}|$ and $|\delta_{LPS}^{LPF}|$ in the range

Optics EXPRESS

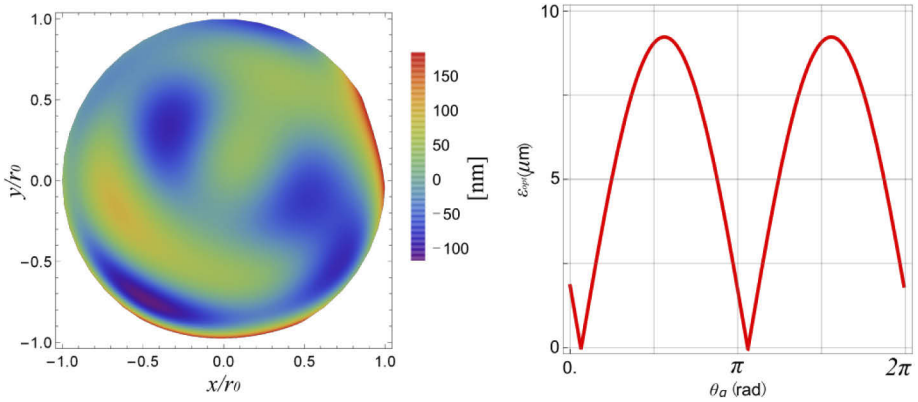

Fig. 5. Left: a randomly generated wavefront. Right: the optimal lateral shift ϵ_{opt} versus the orientation angle of the wavefront tilt θ_α.

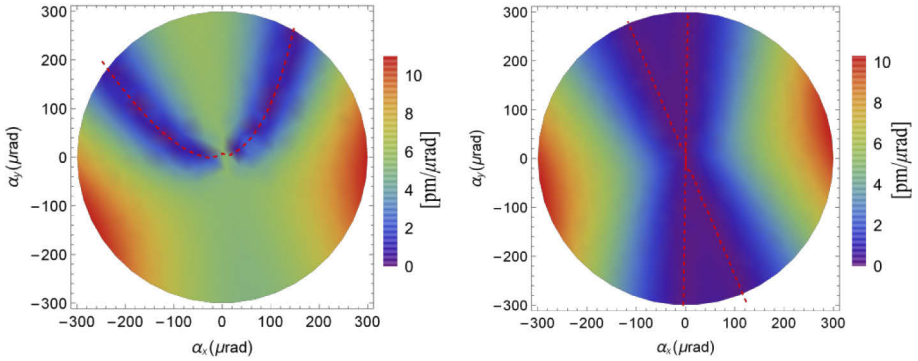

Fig. 6. The coupling coefficient $|\delta^{AP}_{LPS}|$ of the *AP* signal. The red dotted lines indicate the positions with the zero value according to the Eq. (22b). Left: using the Eq. (22a) only. Right: introducing ϵ_{opt} calculated by (23) to (22a).

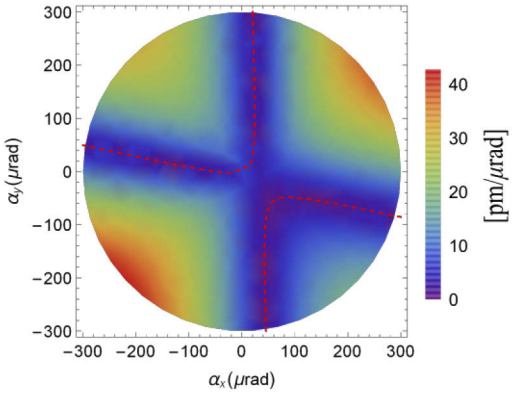

Fig. 7. The coupling coefficient $|\delta^{LPF}_{LPS}|$ of the *LPF* signal according to (21a). The red dotted line indicates the position with the zero value according to (21b).

Optics EXPRESS

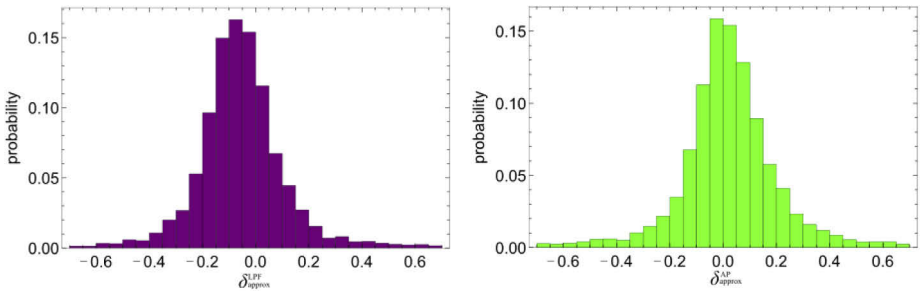

Fig. 8. Histogram of 10^4 Monte Carlo calculation of the residual errors δ^{LPF}_{approx} and δ^{AP}_{approx} when the radius of the flat-top beam and the spot size of the Gaussian beam on the detector $\omega(z) = r_0 = 1mm$. And we set the *RMS* wavefront error $\delta_W = \lambda/10$, the wavefront misalignment $\alpha = 300\mu rad$ and the lateral shift $\epsilon = 60\mu m$ to consider the maximum error.

of $\pm 300\mu rad$ for considering the worst situation. Meanwhile, the corresponding optimal lateral shifts ϵ_{opt} are calculated according to (23). Specifically, as for the *AP* signal, we carry out three cases for different lateral shift vector $\vec{\epsilon}$. Among them, case 1 is that $\epsilon = \epsilon_{opt}$ and $\theta_\epsilon = \theta_\alpha$ to consider the compensation mechanism of the lateral shift, case 2 is that $\epsilon = 0$ to assume the perfect centering, and case 3 is that ϵ and θ_ϵ are randomly generated in the range of $\pm 20\mu m$ and $0 \sim 2\pi$, respectively, to consider the position error. Meanwhile, we use case 4 to represent the *LPF* signal.

Figure 9 illustrates the simulation results and Table 2 shows the mean values and the proportions of $|\delta_{LPS}|$ less than the required $25pm/\mu rad$ in the samples of the four cases. Providing that $\delta_W = \lambda/40$, we can notice that most of all samples of all the cases meet the required $25pm/\mu rad$. When $\delta_W = \lambda/20$, although the mean values of all the cases are less than the required $25pm/\mu rad$ and the samples of the three cases of *AP* signal nearly fulfill the requirement, the proportion of samples satisfying the requirement for the *LPF* signal is reduced to 55%. If δ_W rises to $\lambda/10$, only the samples of the case 1 can nearly meet the requirement. And in general, we can also notice that ϵ_{opt} increases with the deterioration of the wavefront quality.

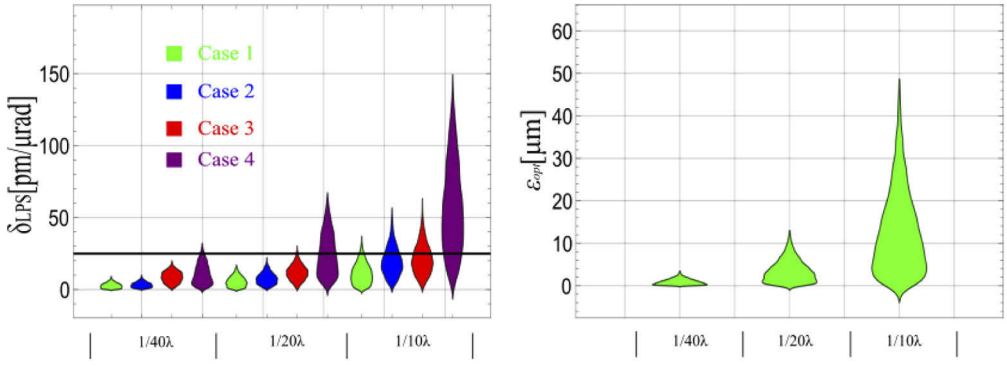

Fig. 9. In the wavefront error δ_W of $\lambda/40$, $\lambda/20$ and $\lambda/10$. Left: the sample distributions of the coupling coefficient $|\delta_{LPS}|$ of the four cases. Right: the sample distributions of the optimal lateral shift ϵ_{opt} in the case 1.

Finally, in the range of $0 \sim \lambda/10$ and the step of $\lambda/100$ for δ_W, we repeat the above calculation process. As shown in Fig. 10, the data points are linked into lines, respectively. The results indicate that provided that δ_W is less than $\lambda/50$, the mean value of δ_{LPS} for the case 3 is slightly larger than other cases because of the term $P_1^{\epsilon 1}$ concerning the lateral shift ϵ_r. But with the

Optics EXPRESS

Table 2. The specific mean values and the proportions of $|\delta_{LPS}|$ less than the required $25pm/\mu rad$ in the samples of the four cases when δ_W is $\lambda/40$, $\lambda/20$ and $\lambda/10$, respectively.

$\delta_{LPS}[pm/\mu rad]$ \ $\delta_W[\lambda]$ / Case	1/40		1/20		1/10	
	Mean	Proportion (<25)	Mean	Proportion (<25)	Mean	Proportion (<25)
Case 1	2.61	100%	5.26	100%	10.61	95.4%
Case 2	3.11	100%	7.42	100%	18.71	72.3%
Case 3	8.61	100%	11.65	98.7%	20.53	65.4%
Case 4	9.84	96.7%	22.64	55.4%	53.85	15.7%

increase of δ_W, the difference between the case 2 and the case 3 is getting smaller, which indicates that the random deviation within ±20 microns for the lateral eccentricity of the interfering beams at the detector has a limited effect on the *AP* signal. Meanwhile, the mean value of $|\delta_{LPS}|$ and the number of samples that do not meet the requirement for the *LPF* signal, increase faster than the other *AP* signals. Among them, case 1 performs best for reducing the TTL noise coupled with aberrations. Correspondingly, the mean value and the maximum value of the optimal lateral shift, increase from 0 to $12.8\mu m$ and from 0 to $59.5\mu m$, respectively, while δ_w increases from 0 to 0.1λ.

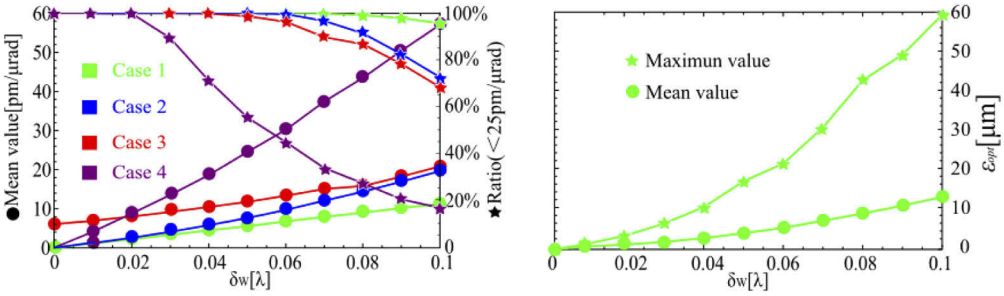

Fig. 10. In the range of $0 \sim \lambda/10$ and the step of $\lambda/100$ for δ_W. Left: the specific mean values and the proportions of $|\delta_{LPS}|$ less than the required $25pm/\mu rad$ in the samples of the four cases versus δ_W. Right: the specific mean values and maximum values of the optimal lateral shift ϵ_{opt} versus δ_W in the case 1.

5. Conclusion

Owing to the tilts and jitters of the spacecraft and angular amplification of the telescope, the received beam is misaligned and jittered to interference with the local beam. As a result, the wavefront aberrations of the interfering beams can couple with the jitter and generate the TTL noise.

In this paper, we first construct the optical model of the phase noise under the two phase definitions (the *AP* signal and the *LPF* signal), when the flat-top beam and the Gaussian beam interfere in the case of the wavefront tilt, aberrations and eccentricity on the QPD. Then taking into account the spherical aberration and the coma of Seidel aberrations, we carry out the relevant analytical computations to obtain the slightly simpler expressions of the phase noises for the *AP* signal and the *LPF* signal, respectively. Go further, we take advantage of the first 25 terms of the Fringe Zernike polynomials for constituting the wavefront aberrations to obtain the expressions (21a) and (22a) of the coupling coefficients between the TTL noise and aberrations. Meanwhile, we analytically derive the expression (23) of the optimal lateral shift which can reduce the coupling degree between the TTL noise and aberrations for the *AP* signal.

Optics EXPRESS

On the above bases, we implement Monte Carlo algorithm to generate arbitrary 10^4 samples for different *RMS* wavefront aberrations in the range of $0 \sim \lambda/10$. Finally, we set $\omega(z) = r_0 = 1mm$ to estimate the coupling coefficients for the *LPF* signal, and the *AP* signals with three different lateral shifts (zero, random in the range of $\pm 20\mu m$, and the optimal) of the interfering beams on the detector. And considering Murphy's law, we optimize the wavefront tilt in the range of $\pm 300\mu rad$ to take the maximum values of the coupling coefficients.

The results show that only if the *RMS* wavefront error is less than $\lambda/20$, the mean coupling coefficients of the *LPF* signal can be less than the required $25pm/\mu rad$. However, even if the *RMS* wavefront error equals $\lambda/10$, the mean coupling coefficients of the three kinds of *AP* signals are all less than the required $25pm/\mu rad$, and further for the *AP* signal introducing the optimal lateral shift, the proportion of the samples fulfilling the requirement can reach 95.4%. Therefore, we can conclude that the *AP* signal is a better method of the phase definition than the *LPF* signal to suppress the influence of aberration on the TTL noise.

Correspondingly, the Eqs. (22a),(22c) and (22h ~ 22j) suggest that the TTL noise coupled with the coma and the trefoil aberrations can be mostly compensated through introducing the optimal lateral shift. Normally, these aberrations are caused by the lateral alignment errors of the lens or mirrors in the practical optical systems [19,20]. Definitely, it may be difficult to directly adopt the above method for the practical space environment because of the random orientation of pointing jitter, but easy for the ground experiments due to the available orientation of rotating angle, e.g. the phenomena in the experiment [14].

If the fitted Fringe Zernike coefficients of the wavefront error between the interfering beams are available, the analytical results in this paper can be used to predict the TTL coupling noise and calculate the optimal lateral shift between the interfering beams and the QPD to reduce the TTL noise coupled by wavefront aberrations.

Funding

Chinese Academy of Sciences (XDB23030000); the Projects of Science Technology Development Plan of Jilin Province under Grant (20190302102GX).

Disclosures

The author declare no conflicts of interest.

References

1. K. Danzmann, the LI. S. A study team, "LISA: laser interferometer space antenna for gravitational wave measurements," Classical Quantum Gravity **13**(11A), A247–A250 (1996).
2. Z. Luo, Z. Guo, G. Jin, Y. Wu, and W. Hu, "A brief analysis to taiji: Science and technology," Results Phys. **16**, 102918 (2020).
3. Y. Dong, H. Liu, Z. Luo, Y. Li, and G. Jin, "A comprehensive simulation of weak-light phase-locking for space-borne gravitational wave antenna," Sci. China: Technol. Sci. **59**(5), 730–737 (2016).
4. M. Chwalla, K. Danzmann, G. F. Barranco, E. Fitzsimons, O. Gerberding, G. Heinzel, C. J. Killow, M. Lieser, M. Perreur-Lloyd, D. I. Robertson, S. Schuster, T. S. Schwarze, M. Tröbs, H. Ward, and M. Zwetz, "Design and construction of an optical test bed for LISA imaging systems and tilt-to-length coupling," Classical Quantum Gravity **33**(24), 245015 (2016).
5. A. Sutton, K. McKenzie, B. Ware, and D. A. Shaddock, "Laser ranging and communications for lisa," Opt. Express **18**(20), 20759–20773 (2010).
6. D. R. Weise, P. Marenaci, P. Weimer, H. R. Schulte, P. Gath, and U. Johann, "Alternative opto-mechanical architectures for the lisa instrument," J. Phys.: Conf. Ser. **154**, 012029 (2009).
7. Z. Wang, T. Yu, Y. Zhao, Z. Luo, W. Sha, C. Fang, Y. Wang, S. Wang, K. Qi, Y. Wang, and X. Xu, "Research on telescope ttl coupling noise in intersatellite laser interferometry," Photonic Sens. **10**(3), 265–274 (2020).
8. S. Schuster, G. Wanner, M. Tröbs, and G. Heinzel, "Vanishing tilt-to-length coupling for a singular case in two-beam laser interferometers with gaussian beams," Appl. Opt. **54**(5), 1010–1014 (2015).
9. C. Sasso, G. Mana, and S. Mottini, "Coupling of wavefront errors and pointing jitter in the lisa interferometer: misalignment of the interfering wavefronts," Classical Quantum Gravity **35**(24), 245002 (2018).

Optics EXPRESS

10. E. Morrison, B. J. Meers, D. I. Robertson, and H. Ward, "Automatic alignment of optical interferometers," Appl. Opt. **33**(22), 5041–5049 (1994).
11. H.-Z. Duan, Y.-R. Liang, and H.-C. Yeh, "Analysis of non-linearity in differential wavefront sensing technique," Opt. Lett. **41**(5), 914–917 (2016).
12. M. Deprez, C. Bellanger, L. Lombard, B. Wattellier, and J. Primot, "Piston and tilt interferometry for segmented wavefront sensing," Opt. Lett. **41**(6), 1078–1081 (2016).
13. G. Wanner, S. Schuster, M. Tröbs, and G. Heinzel, "A brief comparison of optical pathlength difference and various definitions for the interferometric phase," J. Phys.: Conf. Ser. **610**, 012043 (2015).
14. S. Schuster, "Tilt-to-length coupling and diffraction aspects in satellite interferometry," Ph.D. thesis, Gottfried Wilhelm Leibniz Universität Hannover (2017).
15. C. P. Sasso, G. Mana, and S. Mottini, "Telescope jitters and phase noise in the lisa interferometer," Opt. Express **27**(12), 16855–16870 (2019).
16. Y. Zhao, Z. Wang, Y. Li, C. Fang, and H. Gao, "Method to remove tilt-to-length coupling caused by interference of flat-top beam and gaussian beam," Appl. Sci. **9**(19), 4112 (2019).
17. Y. Zhao, "The mathematica codes for the symbolic calculations and the analysis," figshare (2020) [retrieved 9 May 2020], https://doi.org/10.6084/m9.figshare.12278228.
18. D. Malacara, *Optical shop testing* (John Wiley & Sons, 2007).
19. K. P. Thompson, "Multinodal fifth-order optical aberrations of optical systems without rotational symmetry: the comatic aberrations," J. Opt. Soc. Am. A **26**(5), 1090–1100 (2009).
20. R. Jacob, B. Aaron, P. Kevin, J. Thompson, and P. Rolland, "Freeform spectrometer enabling increased compactness," Light: Sci. Appl. **6**(7), e17026 (2017).